ROYAL SOCIETY
OF CHEMISTRY

PAPER

Check for updates

Enhanced stability of vanadium-doped Li$_{1.2}$Ni$_{0.16}$Co$_{0.08}$Mn$_{0.56}$O$_2$ cathode materials for superior Li-ion batteries†

Miaomiao Zhou,‡[a] Jianjun Zhao, ‡[b] Xiaodong Wang,‡[a] Ji Shen,[a] Jin-Lin Yang,[cd] Wenhao Tang,[a] Yirui Deng,[a] Shi-Xi Zhao [*c] and Ruiping Liu [*a]

Lithium–manganese-based cathode materials have attracted much attention due to its high specific capacity, but the low initial coulomb efficiency, poor rate performance and voltage attenuation during cycling limit its application. In this work, Li$_{1.2}$Ni$_{0.16}$Co$_{0.08}$Mn$_{0.56-x}$V$_x$O$_2$ samples ($x = 0$, 0.005, 0.01, 0.02, 0.05) were prepared using the sol–gel method, and the effects of different V^{5+} contents on the structure, valence state, and electrochemical performance of electrode materials were investigated. The results show that the introduction of high-valence V^{5+} in cathode materials can reduce partial Mn^{4+} to active Mn^{3+} ions for charge conservation, which not only improves the discharge capacity and coulomb efficiency of Li-rich manganese-based cathode materials, but also inhibits the voltage attenuation. The initial discharge capacity of the Li$_{1.2}$Ni$_{0.16}$Co$_{0.08}$Mn$_{0.55}$V$_{0.01}$O$_2$ is as high as 280.9 mA h g^{-1} with coulomb efficiency of 77.7% at 0.05C, which is much higher than that of the undoped pristine sample (236.6 mA h g^{-1} with coulomb efficiency of 74.0%). After 100 cycles at 0.1C, the capacity retention rate of Li$_{1.2}$Ni$_{0.16}$Co$_{0.08}$Mn$_{0.55}$V$_{0.01}$O$_2$ was 92.3% with the median voltage retention rate of 95.6%. This work provides a new idea for high performance of lithium-rich manganese-based cathode materials.

1. Introduction

Lithium-ion batteries (LIBs) have been widely used in different portable electronic devices and electric vehicles due to its high energy density, long cycle life and environment benign, thereby becoming an integral part of our lives.[1–4] As is well known, capacity is determined by the ability to store lithium ions, while the energy density is proportional to the capacity and potential of discharge,[5,6] and thus the cathode materials with layered structure exhibit great advantages and potential for use in new generation of renewable power sources.[7–9] Among them, LiCoO$_2$ with a relative high theoretical specific capacity of 274 mA h g^{-1} is one of the most popular cathode materials, however, the scarcity of cobalt resources, lower actual specific capacity of 140 mA h g^{-1}, the collapse of the structure and lattice distortion

during cycling restrain its widely use.[10–12] Therefore, it is highly desired to explore the new cathode materials with high theoretical specific capacity and low cost.[13–17]

Lithium-rich cathode materials with discharge capacities exceeding 250 mA h g^{-1} and energy densities of reaching 300 W h kg^{-1} have been attracted more attention.[18–20] However, the low diffusion coefficient of lithium ions of lithium-rich cathode materials will lead to poor rate performance, and after the initial loss of oxygen, Li-rich NMC deliver descent capacity and lose energy density due to voltage decay, which is caused by irreversible migration of transition metals into the interlayer space during oxidation, where their redox potential is lower.[21–23] Moreover, the Ni^{4+} ions will migrate to the surface of the materials and undergo severe side reactions with the electrolyte during cycling, which will lead to the reduced redox capacity and instability of interaction between Mn and Ni, and finally result in the voltage attenuation.[24,25] To solve these problems, numerous strategies including surface modification and bulk doping have been proposed.[26–28] Although the dissolution damage of the cathode materials in electrolyte solution can be inhibited by surface modification to some extent, the crystal structure of lithium-rich cathode materials tends to change during high-voltage charging and discharging.[29–31] In contrast, appropriate doping can reinforce the crystal structure to improve the structural stability of materials, meanwhile improve the diffusion coefficient lithium ions in electrode materials,[32,33] and thus it is considered to be a more effective

a School of Chemical & Environmental Engineering, China University of Mining and Technology (Beijing), Beijing, 100083, China. E-mail: lrp@cumtb.edu.cn

b State Key Laboratory of Chemical Resources Engineering, Beijing Advanced Innovation Center for Soft Matter Science and Engineering, College of Chemistry, Beijing University of Chemical Technology, Beijing, 100029, China

c Tsinghua Shenzhen International Graduate School, Tsinghua University, Shenzhen, 518055, China. E-mail: zhaosx@sz.tsinghua.edu.cn

d School of Materials Science and Engineering, Tsinghua University, Beijing, 100084, China

‡ These authors contributed equally to this work.

modification strategy. Up to now, numerous metal cations have been used for doping, such as Fe,[34] Sn,[35] Zr,[36] Ti, Ru,[37] Cr and Al. Fe doping can stabilize the layered structure and improve the rate performance.[38,39] Cr doping can increase the area of the inclined region (below 4.5 V), thereby restrain voltage fading, and consequently, the amount of oxygen evolution above the voltage plateau region (4.5 V) can be decreased.[40] The cycling stability of $Li_{1.2}Mn_{0.56-x}Al_xNi_{0.16}CO_{0.08}O_2$ has been improved by aluminum doping, and in particular, the capacity retention rate of $Li_{1.2}Mn_{0.51}Al_{0.05}Ni_{0.16}Co_{0.08}O_2$ and $Li_{1.2}Mn_{0.48}Al_{0.08}Ni_{0.16}Co_{0.08}O_2$ electrodes are enhanced. However, the lower coulombic efficiency of the untreated material (only 68%),[41] the lower median voltage, and the electrolyte corrosion of the cathode materials are the main issues which further need to explore.[42,43]

Vanadium ions are considered as the most suitable substitute to manganese ions due to their similar ionic radii.[44] Appropriate V doping can reduce the mixing degree of Li/Ni, thus stabilize the structure and improve the electrochemical performance.[45] Herein, $Li_{1.2}Ni_{0.16}Co_{0.08}Mn_{0.56-x}V_xO_2$ samples were prepared by using the sol–gel method. The results show that $Li_{1.2}Ni_{0.16}Co_{0.08}Mn_{0.55}V_{0.01}O_2$ exhibits best electrochemical performance within 2.0–4.8 V at 0.1C rate. After 100 cycles, the discharge specific capacity of 225.66 mA h g^{-1} and the capacity retention rate of as high as 92.3% can be obtained. The median voltage attenuation is only 0.15 V, and the retention rate is 95.6%. The doping of high-valence vanadium cannot only improve the cyclic performance of the lithium-rich cathode material, but also inhibit the voltage attenuation. This work provides a new way for improving the electrochemical performance of Li-rich cathode materials.

2. Experimental section

2.1. Synthesis of materials

A series of V-doped $Li_{1.2}Ni_{0.16}Mn_{0.56-x}Co_{0.08}V_xO_2$ samples (x = 0, 0.005, 0.01, 0.02, 0.05) were prepared by the sol–gel method, which are denoted as pristine, V-0.5%, V-1%, V-2%, and V-5%, respectively. Citric acid was used as a chelating agent and deionized water was used as solvent. Typically, a certain stoichiometric ratio of the solute (lithium acetate, nickel acetate, cobalt acetate, manganese acetate, ammonium metavanadate) was dissolved in water to form transparent solution. Subsequently, a certain amount of citric acid solution was added via continuous stirring until the pH was stable (the molar ratio of citric acid to metal ions is 1 : 1). The solution was transferred to a water bath at 60 °C under stirring for 4 h, and then kept at 95 °C to form the sticky gel after evaporating the water. The $Li_{1.2}Ni_{0.16}Co_{0.08}Mn_{0.56-x}V_xO_2$ electrode materials can be obtained after drying the sticky gel at 120 °C for 24 h, pyrolysis at 500 °C for 5 h and calcining at 900 °C for 16 h in air.

2.2 Characterizations methods

The morphologies of the cathode materials before and after cycling were observed by scanning electron microscopy (JSM-7800F, Tokyo, Japan) and transmission electron microscopy

(TEM-2100, JEOL, Tokyo, Japan). The phase composition of the V-doped $Li_{1.2}Ni_{0.16}Mn_{0.56-x}Co_{0.08}V_xO_2$ cathode materials (x = 0, 0.005, 0.01, 0.02, 0.05) was analyzed by a powder X-ray diffractometer (XRD) at a scan rate of 10 deg min^{-1} in the 2θ range of 10°–80° X-ray photoelectron spectroscopy (XPS) was carried out on a Thermo Fisher K-Alpha with an Al K$_\alpha$ X-ray source. The specific surface area of the material was evaluated by means of the Brunauer–Emmett–Teller (BET) model, based on nitrogen adsorption–desorption isotherm tests performed on a BeiShiDe 3H-2000 PM1 instrument.

2.3 Electrochemical measurements

The 2032 type coin cells were assembled in glove box under argon atmosphere. The cathode was prepared by mixing the $Li_{1.2}Ni_{0.16}Co_{0.08}Mn_{0.56-x}V_xO_2$, carbon black and polyvinylidene fluoride (PVDF) with the mass ratio of 8 : 1 : 1 in the N-methyl-2-pyrrolidone (NMP) to form a uniform slurry firstly, and then the slurry was coated on an aluminum foil and dried overnight at 60 °C in vacuum oven. Lithium foil was used as the counter, the porous polyethylene was selected as the separator, and LiPF$_6$ in the mixture of EC : EMC : DMC = 1 : 1 : 1 by volume was used as the electrolyte. Six cells of each cathode material were prepared for simultaneous testing. The cell performance was evaluated at different rates in the voltage range of 2.0–4.8 V at the room temperature on LAND 2001 battery test system (Wuhan Land, China). CV tests and EIS measurements were carried out on IVIUMnSTAT multichannel electrochemical analyzer in the same voltage range at the scanning rate of 0.1 mV s^{-1} and in the frequency range of 0.01–10000 Hz, respectively.

3. Result and discussion

The XRD patterns of the samples with different amount of vanadium-doping are shown in Fig. 1(a). The main peaks for all samples correspond to the layered LiCoO$_2$ phase structure ($R\bar{3}m$ space group).[46] Among them, two pairs of splitting peaks ((006)/(102) and (108)/(110)) are extremely evident, indicating that both the pristine and vanadium substituted samples exhibit a well-formed layered structure.[47] In addition, a small diffraction peak appears between 20° and 25°, demonstrating the presence of the monoclinic Li$_2$MnO$_3$ phases.[48] Due to the slightly larger ion radius of V^{5+} (0.54 Å) than that of Mn^{4+} (0.53 Å), the c/a values of the samples increase with the increase of doping amount (Table S1†). The vanadium ion occupies the TM (Co, Mn and Ni) layer. Due to the slightly larger ion radius of V^{5+} (0.54 Å) than that of Mn^{4+} (0.53 Å), and it is possible that it occupies the lattice position of manganese ions.[49] Meanwhile, the I_{003}/I_{104} ratios of the V-1% sample are larger than that of the pristine material, indicating that the layered structure is more stable. The Li$_3$VO$_4$ impurity phase can be clearly observed in the V-2% and V-5% samples, which may result in the poor electrochemical performance of the cathode material (Fig. 1(b)).

X-ray photoelectron spectroscopy (XPS) of the pristine and V-1% samples are shown in Fig. 1(c–f) and S1.† The binding energies of Ni 2p$_{2/3}$ and 2p$_{1/2}$ for the corresponding electrodes are 854.6 eV and 872.4 eV, respectively,[50,51] and the distance
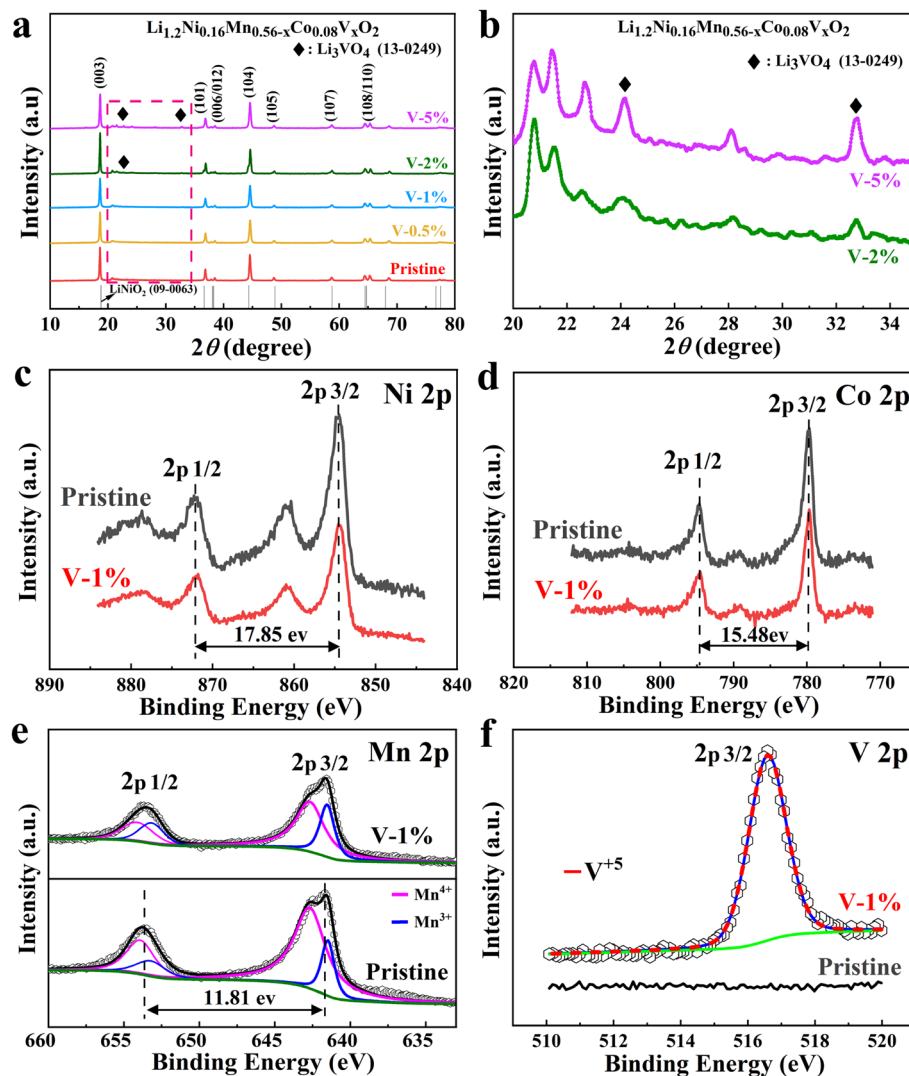
Fig. 1 (a) XRD patterns of samples with different vanadium-doping. (b) XRD patterns of V-2% and V-5% samples at 20°–35°. (c–f) X-ray photoelectron spectroscopy (XPS) of elements (Ni, Co, V, Mn) in pristine ($x = 0$) and V-1% sample.

between binding energy peaks is 17.85 eV,[52] indicates that the valence state of Ni for both samples is +2 (Fig. 1(c)).[53,54] The difference of 15.48 eV between two main peaks of Co $2p_{2/3}$ (780.06 eV) and Co $2p_{1/2}$ (795.54 eV) for the pristine sample are observed, which has been observed previously for Co^{3+} ions (Fig. 1(d)).[55] The V $2p_{2/3}$ peak at 516.58 eV for the V-1% sample demonstrates the successful vanadium doping (Fig. 1(e)). It also should be noted that the percent of Mn^{3+} ions in the V-1% sample is higher (31.67%) than that of pristine material (19.12%), which can be due to the effect of V^{5+} doping (Table S2†). The large charge disbalance in the compound may be ascribed to the concentration difference between the internal and surface of the material, with the surface concentration being greater and the internal concentration being less, which may result in the substitution of Mn^{4+} by V^{5+} having a greater effect on the surface, manifesting as an increase in Mn^{3+} on the surface. When V^{5+} partially replaces Mn^{4+}, a part of Mn^{4+} will transform into Mn^{3+} to keep the valence balance. However, the

difference in Mn^{3+} content between the V-1% and the pristine samples is sufficient to show that some of the Mn^{4+} will be converted to Mn^{3+} to maintain valence equilibrium when V^{5+} partially replaces Mn^{4+}. Generally, Mn^{3+} can contribute capacity due to its electrochemically active characteristic. However, excessive Mn^{3+} will have a negative impact due to the disproportionation reaction of Mn^{3+}, which will produce Mn^{2+} and Mn^{4+}, and Mn^{2+} will dissolve in the electrolyte or migrate to adjacent tetrahedral positions to form a spinel phase. Conversely, Mn^{4+} in the crystal structure is important for ensuring the structural stability of the materials. Therefore, an appropriate ratio of Mn^{3+}/Mn^{4+} has an important effect on the rate and cycle performance of lithium-rich manganese-based cathode materials.[56,57]

Fig. 2 and S2–S4† show the SEM and TEM images of different samples. It can be observed that the primary particles of the pristine material are polygonal spheroids, which exhibit a size of approximately 100–150 nm with a slight agglomeration
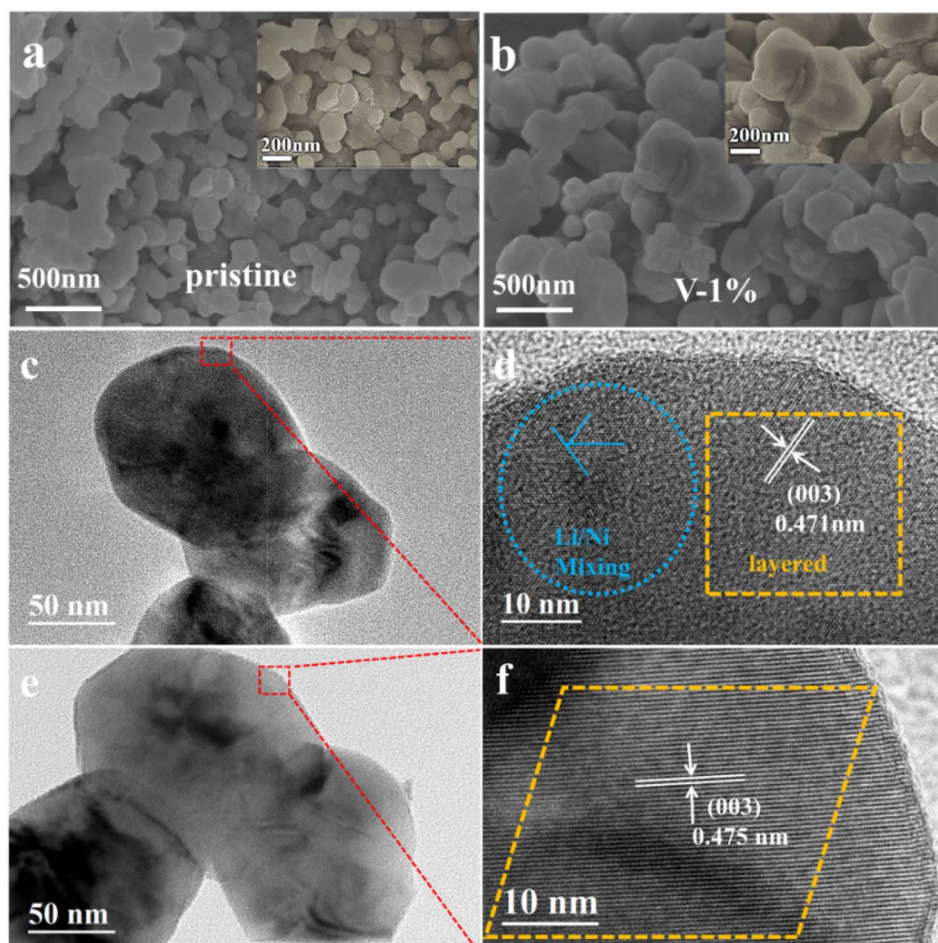
Fig. 2 SEM images of pristine (a) and sample with 1% vanadium doping (b), HRTEM images of pristine (c and d) and sample with 1% vanadium doping (e and f).

(Fig. 2(a)). The addition of element V reduces the agglomeration of the material and lowers the ionic diffusion impedance, while improving the electrical conductivity of the material and accelerating charge transfer, which provides an opportunity for the material to improve its electrochemical performance. As shown in Fig. 2(b), when the doping amount of vanadium is 0.01, the particle size of the sample grows into approximately 200–300 nm, and the uniform distribution of the lithium (yellow), manganese (blue), nickel (purple), cobalt (green), and vanadium (orange) are observed (Fig. S5†), the particle size of the material with 5% vanadium doping is about 100 μm, indicating a severe agglomerate (Fig. S2†). It should be worth noting that V^{5+} cannot be evenly distributed into the lattice of lithium–manganese rich materials when the vanadium doping is larger than 2%. The HRTEM images for the pristine and V-1% samples show that the particle size of the pristine and V-1% samples are similar with a interplanar spacing of 0.475 nm and 0.471 nm (003 reflection), respectively, which is typical for the $R\bar{3}m$ layered structure (Fig. 2(c–f)). No other impurities lattice stripes are observed (Fig. 2(e and f)), which indicates that V is successfully doped into the lattice of the material. The results

verify the high ordering state of the crystal structure, which is consistent with the XRD results.

The size distribution of secondary particles of the pristine, V-1% and V-5% samples is shown in Fig. S6(a and b),† where D90, D50 and D10 are the equivalent diameters (average particle size) of the largest particles in the distribution curve at a cumulative distribution of 90%, 50% and 10%, respectively. It can be observed that the D10, D50, and D90 of the V-1% sample are smaller compared with those of the other two materials, and the particle size is more uniform. According to BET results (Fig. S6(c)†), the surface areas and average pore size of the pristine and sample with 1% vanadium doping are 3.37 $m^2 g^{-1}$/ 13.1 nm and 3.21 $m^2 g^{-1}$/14.5 nm, respectively. It can be assumed that the difference between the particle size for undoped and doped samples is due to the agglomeration of particles, as observed for the V-5% sample.

The initial charge–discharge curves of the pristine, V-0.5%, V-1%, V-2% and V-5% samples in the voltage range of 2.0–4.8 V and at 0.05C rate (1C = 250 mA h g^{-1}) were shown in Fig. S7(a).† All samples showed similar charge–discharge curves, existing slopes and large platform areas, which is similar to other lithium rich manganese based materials. Initial stage (<4.5 V),
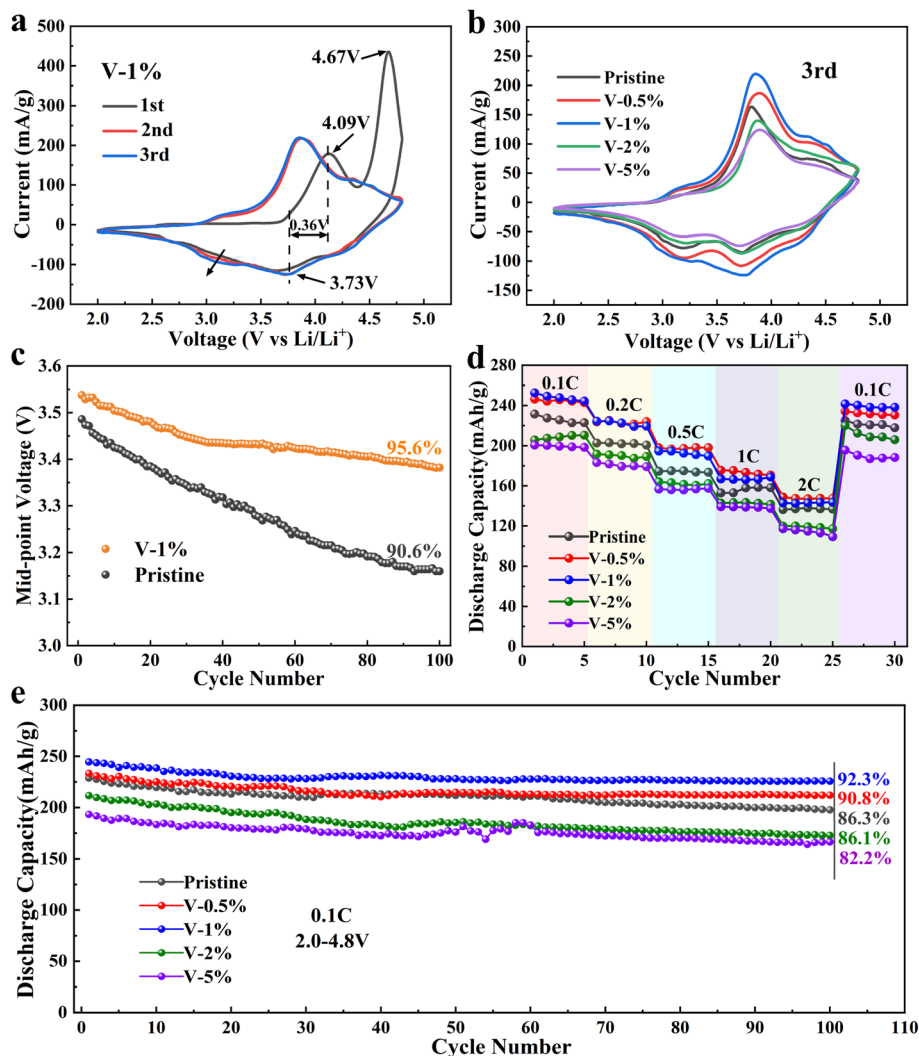
Fig. 3 (a and b) Cyclic voltammetry curves of the pristine, V-0.5%, V-1%, V-2% and V-5% samples at 0.1 mV s^{-1}. (c) Dependence of the average discharge profile on the number of cycles for the Li$_{1.2}$Ni$_{0.16}$Co$_{0.08}$Mn$_{0.56-x}$V$_x$O$_2$ electrodes. (d) The rate and (e) cycling performance of the electrode materials at 0.1C in the range of 2.0–4.8 V.

the Li-ions remove from Li$_2$MnO$_3$ phase and accompanied with the oxidation of transition metal Ni^{2+} to Ni^{3+}, and Co^{3+} to Co^{4+}, in second stage (above 4.5 V), O^{2-} is oxidized to O^{n-} (1 < n< 2), followed by oxidation to O$_2$.[58] With the increase of the amount of V doping, the length of the inclined region increases first and then decreases. As observed, the largest discharge capacity of 134.26 mA h g^{-1} from 2.0 to 4.5 V can be obtained for the V-1% sample, which can be ascribed to the presence of more electrochemically active Mn^{3+} ions, which is in good agreement with the results of the XPS analysis. The total charge/discharge capacity of pristine, V-0.5%, V-1%, V-2% and V-5% are 319.7/236.6 mA h g^{-1}, 348.6/266.2 mA h g^{-1}, 361.6/280.9 mA h g^{-1}, 305.2/223.8 mA h g^{-1} and 296/214.6 mA h g^{-1} respectively, and the initial coulombic efficiency of the materials are 74.1%, 76.3%, 77.7%, 73.3%, and 72.4%, respectively (Table S3†). Furthermore, the discharge voltage platform along the arrow direction decreases with the increase of the number of cycles, and the sample V-1% exhibits the minimum capacity fading,

while too much vanadium doping will cause rapid voltage decay.

Cyclic voltammetry curves for Li$_{1.2}$Ni$_{0.16}$Co$_{0.08}$Mn$_{0.56-x}$V$_x$O$_2$ (x = 0, 0.005, 0.01, 0.02, 0.05) electrode materials are presented in Fig. 3(a and b) and S8.† The oxidation peak at 4.1 V of the all the sample can be ascribed to the oxidation reactions of Ni^{2+} → Ni^{4+} and Co^{3+} → Co^{4+}, and the oxidation peak at 4.72 V corresponds to the oxidization of O^{2-} to O^{n-} (1 < n < 2), followed by oxidation to O$_2$. Three reduction peaks, corresponding to the reduction of Ni^{4+}, Co^{4+} and Mn^{4+}, are observed in the first cycling process for all electrode materials.[59,60] Compared to the first cycle, the sharp oxidation peak at 4.72 V disappears in the subsequent cycles, which can be attributed to an excessive Li$^+$ remove from layered Li$_2$MnO$_3$ and an irreversible lattice oxygen escape, and finally resulting in a large irreversible capacity loss in the initial charge/discharge cycle. As the number of cycles increase, a new reduction peak around 3.1 V appears during the negative sweep, which corresponds to the reduction of Mn^{4+} to
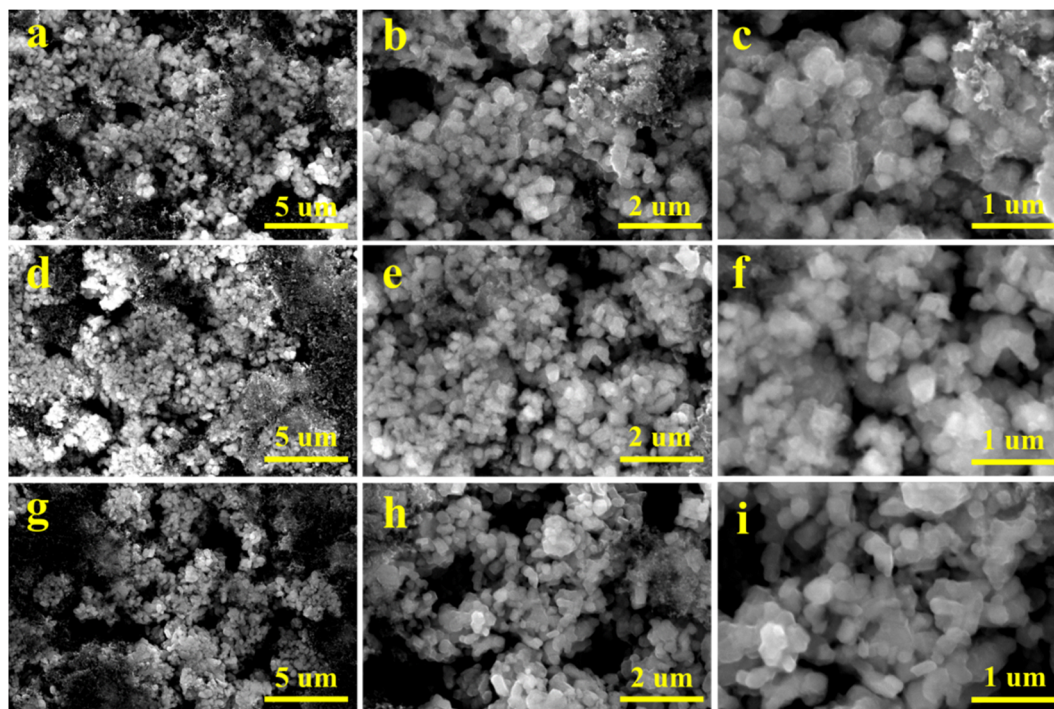
RSC Advances

Paper

Fig. 4 SEM images of the pristine (a–c), V-1% (d–f) and V-5% (g–i) samples after 100 cycles at 0.1C (1C = 250 mA g^{-1}).

Mn^{3+} and the gradual transformation of the layered phase to the spinel phase.[61] It should be noted that the reduction peak of the V-1% sample (at approximately 3.1 V) changes insignificantly from the first cycle to the third cycle, which proves that a proper amount of V doping can inhibit the conversion of the layered structure to the spinel structure and improve the structural stability of the material. Furthermore, appropriate V doping can reduce the polarization of REDOX, and the smallest potential difference of 0.36 V can be obtained in the V-1% sample. Moreover, the cyclic voltammetry curves of the V-1% sample was

well overlapped with an increase in the number of cycles, indicating the good reversibility of the materials.

Fig. 3(c) shows that the median voltage of the pristine and the V-1% samples decrease as the number of cycles increases. The voltage decay of the pristine sample is evidently faster, especially in the first few cycles, and it can be ascribed to the phase transition of the cathode materials during charging/discharging. The median voltage of the samples with vanadium doping is higher, which can be due to the improvement of the structural stability of the material. The drop in the average
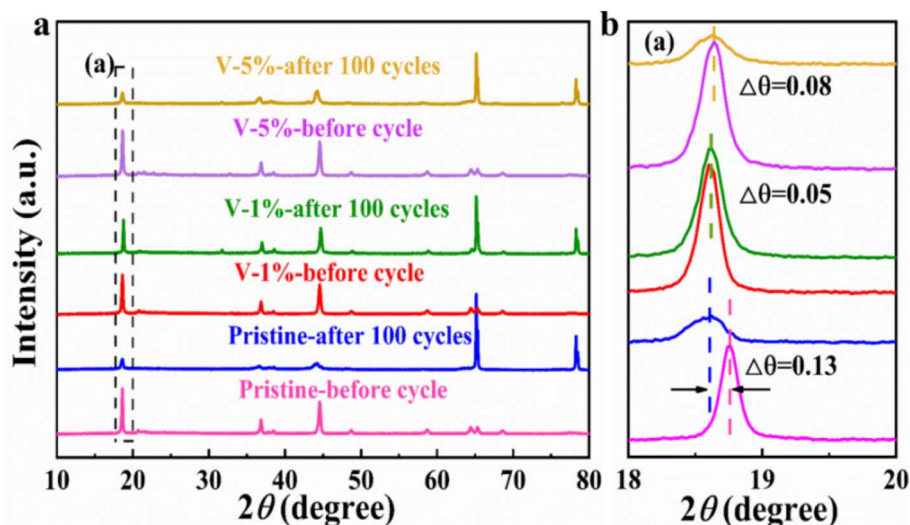

Fig. 5 (a) XRD patterns of the pristine, V-1% and V-5% samples after 100 cycles at 0.1C (1C = 250 mA h g^{-1}); (b) magnified view of the XRD patterns at 18°–20°.
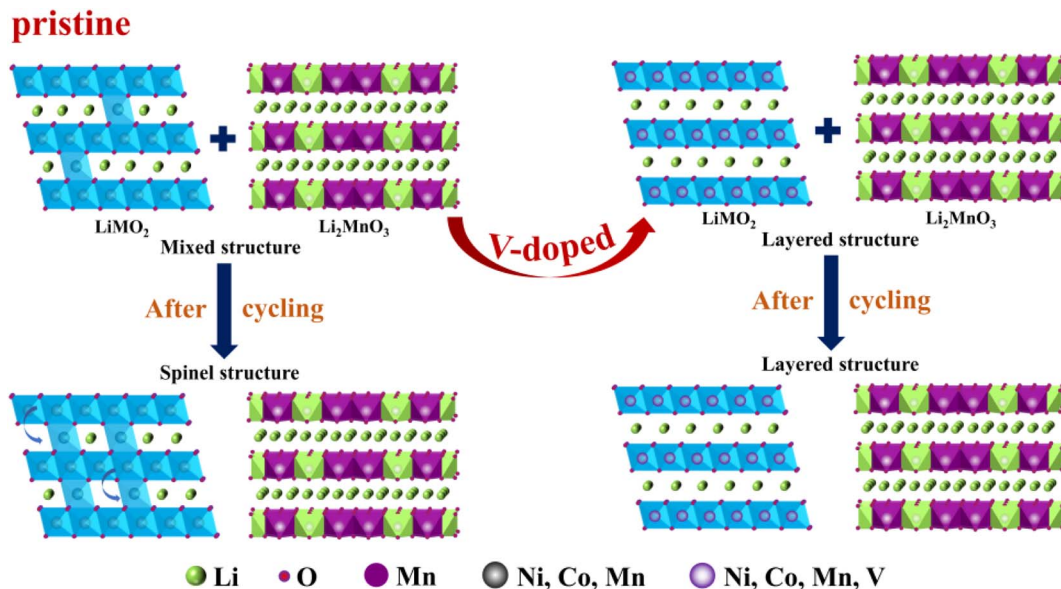
Fig. 6 Schematic illustration of structural transformation of the cathode materials during the cycling.

discharge voltage is 0.400, 0.390, 0.156, 0.332 and 0.388 V for pristine, V-0.5%, V-1%, V-2% and V-5%, respectively. It can be concluded that an appropriate amount of V doping can improve the structural stability of the lithium–manganese rich layered oxide and inhibit the transformation of the layered structure to the spinel structure.

The rate performance of the pristine sample and the V-0.5%, V-1%, V-0.2%, V-2% and V-5% samples is evaluated at 0.1, 0.2, 0.5, 1 and 2C in the voltage range of 2.0–4.8 V for 5 cycles (Fig. 3(d)). The results show that the rate performance of the sample doped with 1% of V is better than that of the original sample, but excessive doping has the negative effect. The discharge capacity of the pristine, V-1% and V-5% samples is 168.65 mA h g^{-1}, 158.13 mA h g^{-1} and 137.37 mA h g^{-1} at 1C, respectively. The highest discharge capacity of 238.5 mA h g^{-1} for the V-1% sample can be restored when the current density goes back to 0.1C, while the sample with 5% vanadium doping deliver the minimum discharge capacity of 188.27 mA h g^{-1}, and it may be attributed to the formation of the LiV$_3$O$_4$ heterogeneous phase, which will greatly reduce the conductivity of the material. As shown in Fig. 3(e), after 100 charge/discharge cycles at 0.1C, the capacity retention of V-1% electrodes (92.3%) is much higher than that of the pristine (85.1%), V-0.5% (90.8%), V-2% (82.2%) and V-5% (86.1%) electrodes, which further indicates the improved structural stability of the electrode after doping with 1% vanadium.

The electrochemical impedance spectra of all samples after 3rd and 100th cycles are shown in Fig. S9.† The semicircle in the high frequencies region corresponds to the battery's ohmic resistance (R_s) and charge transfer resistance (R_{ct}) at the electrode/electrolyte interface, and the slope in the low-frequency region corresponds to the Warburg impedance associated with Li$^+$ diffusion in the bulk materials, and the CPE is the capacitance of the electrode/electrolyte bilayer. The EIS

spectrum after the third cycle showed that the charge transfer resistance decreased linearly with the increase of doping amount of vanadium, and then increased significantly (Table S4†). The charge transfer resistance across the electrolyte/ intercalate interface (R_{ct}) of the pristine, V-0.5%, V-1%, V-2% and V-5% samples is 49.85, 45.15, 14.61, 105.9 and 113.5 Ω, respectively. A decrease in R_{ct} indicates a significant effect of vanadium doping on the transport rate of lithium ions through the electrode/electrolyte interface. This behavior is observed when the vanadium content increases up to 1%, which confirms the earlier assumption that the crystal structure is stabilized by doping with vanadium ions. At the same time, excessive doping leads to the formation of an impurity phase and the agglomeration of particles. The increase in particle agglomeration leads to a decrease in the solid phase diffusion coefficient and electron conductivity, an increase in the internal resistance of the cell and an increase in the charge transfer impedance.

To further study the influence of vanadium doping on the morphology of the material, SEM images of the pristine, V-1% and V-5% samples after 100 cycles were obtained (Fig. 4). The particles of the pristine material are evidently damaged with rough surfaces and rounded edges after cycling. The lithium-rich manganese based electrode materials can react with the electrolyte during subsequent cycling processes, which result in the destroyed structure of the material. The sample with 5% vanadium doping also tends to pulverization due to the corrosion of the electrolyte. Compared with that of the pristine and V-5% samples, the morphology of the V-1% material is integrity and smooth, which is benefit from the stabilization of the internal structure of the material by a small amount of vanadium doping.

The crystal structures of the pristine, V-1% and V-5% samples before and after 100 cycles can be clearly observed in Fig. 5. LiMn$_2$O$_4$ phase with *Fd̄m* space group appears for all

materials, indicating that the crystal structure of the electrode is changed, and the new spinel phase is formed due to the structural rearrangement of certain layered compositions during charge–discharge process (Fig. 5(a)). Thus, a decrease in the diffraction intensity of the (003) peak occurs due to the transformation of the layered structure to a spinel structure during cycling. As shown in Fig. 5(b), owing to an axis expansion after cycling, the (003) diffraction peak was shifted to the low angle by 0.13°, 0.05° and 0.08° for the pristine, V-1% and V-5% samples, respectively. Among them, the V-1% sample exhibits the least deviation in the diffraction angle after cycling, indicating the improved structure stability of the material. Similar to the results before cycling, as shown in Table S5,† the degree of cation mixing of the V-1% samples remained lower than that of the original samples after cycling, indicating that proper V-doping can enhance the structural stability of the Li-rich cathode material.

The structural transformation diagram of the cathode materials is shown in Fig. 6. The structures of the Li-rich samples are composed of LMO$_2$ and Li$_2$MnO$_3$ phases. During cycling, part of Li ions escape from the LMO$_2$ lattice and enter into the Li$_2$MnO$_3$ lattice, meanwhile, some transition metal ions may occupy the position of Li$^+$ in the Li layers, resulting in local areas TM/Li mixing in the domain, and finally leading to the two-phase coexistence of layered structure ($R\bar{3}m$) and spinel structure ($Fd\bar{3}m$). After vanadium doping with the appropriate content, a large number of transition metal ions is relatively stable and will not entered into the lithium layer structure.[62] Thus it can stabilize the layered structure to some extent and improve the electrochemical performance of lithium-rich cathode materials.

4. Conclusions

In this work, lithium rich Li$_{1.2}$Ni$_{0.16}$Co$_{0.08}$Mn$_{0.56-x}$V$_x$O$_2$ cathode materials with different amount of vanadium doping were successfully synthesized *via* sol–gel method. The as-obtained lithium-rich manganese-based materials with 1% of V doping exhibit pure $R\bar{3}m$ phase layered structure, uniform particle size without agglomeration. The introduction of V^{5+} into the cathode materials can not only reduce some of the Mn^{4+} to active Mn^{3+} ions, but also decrease the particle size of the as-obtained materials, which is very favorable for Li$^+$ transport and accelerating of the electrochemical reaction kinetics, and thus improves the cycling stability and coulombic efficiency of lithium-rich manganese-based cathode materials. The appropriate amount of V doping improves the structural stability of the Li–Mn-rich layered oxide, reduces the degree of cation mixing and inhibits the conversion of the layered structure to a spinel structure. Sample V-1% showed a 5% increase in median voltage retention after 100 cycles at 0.1C, indicating that a moderate amount of V doping can also slow down the decay of the median voltage. This work provides a new way to stabilize the lithium-rich manganese-based cathode material during cycling and makes it a promising candidate for high specific energy LIBs.

Conflicts of interest

The authors declare that they have no known competing financial interests or personal relationships that could have appeared to influence the work reported in this paper.

Acknowledgements

References

1 Y. Shao-Horn, L. Croguennec, C. Delmas, E. C. Nelson and M. A. O'Keefe, *Nat. Mater.*, 2003, **2**, 464–467.

2 D. Lin, Y. Liu and Y. Cui, *Nat. Nanotechnol.*, 2017, **12**, 194–206.

3 Y. Wang and S. Zhao, *J. Wuhan Univ. Technol. Mater. Sci. Ed.*, 2016, **31**, 945–949.

4 D. Li, B. Zhang, X. Qu, J. Zhang, K. Meng, G. Ji, P. Li and J. Xu, *Chin. Chem. Lett.*, 2021, **30**, 2333–2337.

5 Y.-K. Sun, S.-T. Myung, B.-C. Park, J. Prakash, I. Belharouak and K. Amine, *Nat. Mater.*, 2009, **8**, 320–324.

6 Y. X. Xie, S. Z. Chen, W. Yang, H. B. Zou, Z. Y. Lin and J. C. Zhou, *J. Alloy Compd.*, 2019, **772**, 230–239.

7 P. Wu, B. Shi, H. Tu, C. Guo, A. Liu, G. Yan and Z. Yu, *J. Adv. Ceram.*, 2021, **10**, 1129–1139.

8 Y. Ding, D. Mu, B. Wu, R. Wang, Z. Zhao and F. Wu, *Appl. Energy*, 2017, **195**, 586–599.

9 Q. Wang, H. Zhao, B. Li, C. Yang, M. Li, Y. Li, P. Han, M. Wu, T. Li and R. Liu, *Chin. Chem. Lett.*, 2021, **32**, 1157–1160.

10 M. Zhou, *Int. J. Electrochem. Sci.*, 2020, 10759–10771.

11 T. Ohzuku and A. Ueda, *J. Electrochem. Soc.*, 1994, **141**, 2972–2977.

12 C. Y. Cui, X. L. Fan, X. Q. Zhou, J. Chen, Q. C. Wang, L. Ma, C. Y. Yang, E. Y. Hu, X. Q. Yang and C. S. Wang, *J. Am. Chem. Soc.*, 2020, **142**, 8918–8927.

13 Q. Zhang, Y. He, G. Lin, X. Ma, Z. Xiao, D. Shi and Y. Yang, *J. Mater. Chem. A*, 2021, **9**, 10652–10660.

14 X. Wu, S. X. Zhao, L. Wei, H. Deng and C. W. Nan, *J. Alloy Compd.*, 2018, **735**, 1158–1166.

15 F. Yang, X. Feng, Y. S. Liu, L. C. Kao, P. A. Glans, W. Yang and J. Guo, *Energy Environ. Mater.*, 2021, **4**, 139–157.

16 W. Xu and Y. Wang, *Ionics*, 2018, **24**, 2523–2532.

17 L. Zhu, Y. Liu, W. Wu, X. Wu, W. Tang and Y. Wu, *J. Mater. Chem. A*, 2015, **3**, 15156–15162.

18 B. Li, X. Wang, Y. Gao, B. Wang, J. Qiu, X. Cheng and D. Dai, *J. Materiom*, 2019, **5**, 149–155.

19 Z. Yang, C. Zheng, Z. Wei, J. Zhong, H. Liu, J. Feng, J. Li and F. Kang, *Energy Mater.*, 2022, **2**, 200006.

20 K. Mu, Y. Cao, G. Hu, K. Du, H. Yang, Z. Gan and Z. Peng, *Electrochim. Acta*, 2018, **273**, 88–97.

21 T. Liu, S.-X. Zhao, L.-L. Gou, X. Wu and C.-W. Nan, *Rare Met.*, 2019, **38**, 189–198.

22 K. Bi, S. X. Zhao, C. Huang and C. W. Nan, *J. Power Sources*, 2018, **389**, 240–248.

23 Y. Shang, T. Chu, B. Shi and K. Fu, *Energy Environ. Mater.*, 2020, **4**, 213–221.

24 P. Hou, J. Yin, M. Ding, J. Huang and X. Xu, *Small*, 2017, **13**, 201701802.

25 W. Huang, W. Li, L. Wang, H. Zhu, M. Gao, H. Zhao, J. Zhao, X. Shen, X. Wang, Z. Wang, C. Qi, W. Xiao, L. Yao, J. Wang, W. Zhuang and X. Sun, *Small*, 2021, **17**, 202104282.

26 J. Zhang, H. Zhang, R. Gao, Z. Li, Z. Hu and X. Liu, *Phys. Chem. Chem. Phys.*, 2016, **18**, 13322–13331.

27 R. Tatara, Y. Yu, P. Karayaylali, A. K. Chan, Y. Zhang, R. Jung, F. Maglia, L. Giordano and Y. Shao-Horn, *ACS Appl. Mater. Interfaces*, 2019, **11**, 34973–34988.

28 R. Sharpe, R. A. House, M. J. Clarke, D. Forstermann, J. J. Marie, G. Cibin, K. J. Zhou, H. Y. Playford, P. G. Bruce and M. S. Islam, *J. Am. Chem. Soc.*, 2020, **142**, 21799–21809.

29 J. Zheng, Y. Xie, S. S. Jiang, Y. Z. Long, X. Ning and Z. G. Lan, *Phys. Chem. Chem. Phys.*, 2019, **21**, 26502–26514.

30 Z. Yang, J. J. Zhong, J. L. Li, Y. Y. Liu, B. B. Niu and F. Y. Kang, *Ceram. Int.*, 2019, **45**, 439–448.

31 Y. L. Heng, Z. Y. Gu, J. Z. Guo, X. T. Wang, X. X. Zhao and X. L. Wu, *Energy Mater.*, 2022, **2**, 200017.

32 Y. Zhao, J. Liu, S. Wang, R. Ji, Q. Xia, Z. Ding, W. Wei, Y. Liu, P. Wang and D. G. Ivey, *Adv. Funct. Mater.*, 2016, **26**, 4760–4767.

33 S. Y. Zheng, K. Zhou, F. Zheng, H. D. Liu, G. M. Zhong, W. H. Zuo, N. B. Xu, G. Zhao, M. Z. Luo, J. Wu, C. Y. Zhang, Z. R. Zhang, S. Q. Wu and Y. Yang, *ACS Appl. Mater. Interfaces*, 2020, **12**, 40347–40354.

34 J. Billaud, D. Sheptyakov, S. Sallard, D. Leanza, M. Talianker, J. Grinblat, H. Sclar, D. Aurbach, P. Novák and C. Villevieille, *J. Mater. Chem. A*, 2019, **7**, 15215–15224.

35 C. S. Yoon, M. J. Choi, D. W. Jun, Q. Zhang, P. Kaghazchi, K. H. Kim and Y. K. Sun, *Chem. Mater.*, 2018, **30**, 1808–1814.

36 X. Feng, Y. R. Gao, L. B. Ben, Z. Z. Yang, Z. X. Wang and L. Q. Chen, *J. Power Sources*, 2016, **317**, 74–80.

37 B. H. Song, M. O. Lai and L. Lu, *Electrochim. Acta*, 2012, **80**, 187–195.

38 G. R. Hu, Z. C. Xue, Z. Y. Luo, Z. D. Peng, Y. B. Cao, W. G. Wang, Y. X. Zeng, Y. Huang, Y. Tao, T. F. Li, Z. Y. Zhang and K. Du, *Ceram. Int.*, 2019, **45**, 10633–10639.

39 X. Liu, T. Huang and A. Yu, *Electrochim. Acta*, 2014, **133**, 555–563.

40 B. H. Song, C. F. Zhou, H. L. Wang, H. W. Liu, Z. W. Liu, M. O. Lai and L. Lu, *J. Electrochem. Soc.*, 2014, **161**, A1723–A1730.

41 P. K. Nayak, J. Grinblat, M. Levi, O. Haik, E. Levi, S. Kim, J. W. Choi and D. Aurbach, *ChemElectroChem*, 2015, **2**, 1957–1965.

42 P. M. Gonzalez Puente, S. Song, S. Cao, L. Z. Rannalter, Z. Pan, X. Xiang, Q. Shen and F. Chen, *J. Adv. Ceram.*, 2021, **10**, 933–972.

43 X. Wu, X. Liang, X. Zhang, L. Lan, S. Li and Q. Gai, *J. Adv. Ceram.*, 2021, **10**, 347–354.

44 Y. Zang, X. Sun, Z. F. Tang, H. F. Xiang and C. H. Chen, *RSC Adv.*, 2016, **6**, 30194–30198.

45 C. Lu, S. Yang, H. Wu, Y. Zhang, X. Yang and T. Liang, *Electrochim. Acta*, 2016, **209**, 448–455.

46 L. Y. Bao, L. Wei, N. T. Fu, J. Y. Dong, L. Chen, Y. F. Su, N. Li, Y. Lu, Y. J. Li, S. Chen and F. Wu, *J. Energy Chem.*, 2022, **66**, 123–132.

47 Y. Y. He, S. Wang, H. Y. Zhang, X. Chen, J. Li, H. Y. Xu, Y. H. Zhang, K. H. Hu, G. P. Lv, Y. Meng and W. Xiang, *J. Colloid Interface Sci.*, 2022, **607**, 1333–1342.

48 Y. Xie, Y. C. Jin and L. Xiang, *Particuology*, 2022, **61**, 1–10.

49 T. Nakamura, K. Ohta, X. Hou, Y. Kimura, K. Tsuruta, Y. Tamenori, R. Aso, H. Yoshida and K. Amezawa, *J. Mater. Chem. A*, 2021, **9**, 3657–3667.

50 Z.-Y. Kou, Y. Lu, C. Miao, J.-Q. Li, C.-J. Liu and W. Xiao, *Rare Met.*, 2021, **40**, 3175–3184.

51 E. Y. Zhao, M. H. Zhang, X. L. Wang, E. Y. Hu, J. Liu, X. Q. Yu, M. Olguin, T. A. Wynn, Y. S. Meng, K. Page, F. W. Wang, H. Li, X. Q. Yang, X. J. Huang and L. Q. Chen, *Energy Storage Mater.*, 2020, **24**, 384–393.

52 P. P. Zhang, X. H. Zhai, H. Huang, J. F. Zhou, X. B. Li, Y. P. He and Z. C. Guo, *Ceram. Int.*, 2020, **46**, 24723–24736.

53 M. C. Biesinger, B. P. Payne, A. P. Grosvenor, L. W. M. Lau, A. R. Gerson and R. S. Smart, *Appl. Surf. Sci.*, 2011, **257**, 2717–2730.

54 X. Yuan, A. A. Razzaq, Y. Chen, Y. Lian, X. Zhao, Y. Peng and Z. Deng, *Chin. Chem. Lett.*, 2021, **32**, 890–894.

55 R. A. House, G. J. Rees, M. A. Perez-Osorio, J. J. Marie, E. Boivin, A. W. Robertson, A. Nag, M. Garcia-Fernandez, K. J. Zhou and P. G. Bruce, *Nat. Energy*, 2020, **5**, 777–785.

56 S. Ramakrishnan, B. Park, J. Wu, W. L. Yang and B. McCloskey, *J. Am. Chem. Soc.*, 2020, **142**, 8522–8531.

57 Z. Wang, H.-Q. Lu, Y.-P. Yin, X.-Y. Sun, X.-T. Bai, X.-L. Shen, W.-D. Zhuang and S.-G. Lu, *Rare Met.*, 2017, **36**, 899–904.

58 G. Assat, D. Foix, C. Delacourt, A. Iadecola, R. Dedryvère and J.-M. Tarascon, *Nat. Commun.*, 2017, **8**, 2219.

59 A. J. Naylor, I. Kallquist, D. Peralta, J. F. Martin, A. Boulineau, J. F. Colin, C. Baur, J. Chable, M. Fichtner, K. Edstrom, M. Hahlin and D. Brandell, *ACS Appl. Energy Mater.*, 2020, **3**, 5937–5948.

60 Q. He, B. Yu, Z. Li and Y. Zhao, *Energy Environ. Mater.*, 2019, **2**, 264–279.

61 Z. P. Shi, Q. W. Gu, L. Yun, Z. N. Wei, D. Hu, B. Qiu, G. Z. Chen and Z. P. Liu, *J. Mater. Chem. A*, 2021, **9**, 24426–24437.

62 Q. Ma, R. Li, R. Zheng, Y. Liu, H. Huo and C. Dai, *J. Power Sources*, 2016, **331**, 112–121.